Observation of short-lived laser-dressed quantum states in the frequency plane

M. Žitnik,[1] A. Mihelič,[1] K. Bučar,[1] M. Hrast,[1,2] Ž. Barba,[1] Š. Krušič,[1,2] P. Rebernik Ribič,[3,4] J. Urbančič,[4] B. Ressel,[4] M. Stupar,[4] L. Poletto,[5] M. Coreno,[6] D. Gauthier,[7] and G. De Ninno[4,3]

[1]*J. Stefan Institute, Jamova cesta 39, SI-1000 Ljubljana, Slovenia*

[2]*Faculty of Mathematics and Physics, University of Ljubljana, Jadranska 19, SI-1000 Ljubljana, Slovenia*

[3]*Elettra-Sincrotrone Trieste, Strada Statale 14-km 163,5, 34149 Basovizza, Trieste, Italy*

[4]*Laboratory of Quantum Optics, University of Nova Gorica, 5001 Nova Gorica, Slovenia*

[5]*Institute for Photonics and Nanotechnologies, IFN-CNR, 35131 Padova, Italy*

[6]*Institute of Structure of Matter, ISM-CNR, 34149 Basovizza, Italy*

[7]*LIDYL, CEA, CNRS, Université Paris-Saclay, CEA-Saclay, 91191 Gif-sur-Yvette, France*

(Received 24 December 2018; revised manuscript received 7 May 2019; published 28 May 2019)

We present a method for measuring a complete frequency map of laser-dressed states with femtosecond lifetimes. It is based on collecting decay products as a function of the frequency of the excitation pulse and its delay with respect to the linearly chirped laser pulse, centered at the resonant transition frequency. The method has been tested on the case of laser-coupled $2s2p\ ^1P^o$ and $2p^2\ ^1S^e$ autoionizing resonances in He and is applicable to other quantum systems with short-lived states. When the laser coupling effects are known, the excitation pulse properties can be extracted from the map.

DOI: 10.1103/PhysRevA.99.053423

I. INTRODUCTION

A transient quantum state can be modified in a controlled way by coupling it to one or several of the neighboring states with a laser. Under the influence of a strong electromagnetic field, the states of, e.g., an atom, a molecule, or a crystal, are "dressed" by the field. The properties of these states depend on the field intensity, frequency, and polarization [1]. The physics of a pair of states coupled by a laser is well known [2], and leads to the Autler-Townes doublet [3], with the characteristic energy splitting given by $\sqrt{\Omega^2+\delta^2}$, where Ω denotes the driving (Rabi) frequency and δ the detuning from the resonant frequency. On resonance ($\delta = 0$), each of the dressed states takes half of the original excitation strength and the Autler-Townes splitting (ATS) equals the Rabi frequency. A direct result of the ATS is reduced target absorption in the spectral gap of the doublet where the transmission is also modulated by the quantum interference effect known as electromagnetically induced transparency [4]. These phenomena have a rich variety of applications including dissipation-free light transmission and fast low-power optical switching [5]. They enable a control of decay branching ratios, measurements of transition dipole moments, electromagnetic field characterization [6], and offer a framework for single-qubit operations relying solely on optical fields [7].

The simplest manifestation of the laser coupling is therefore a change in the transmission or reflection of the excitation pulse upon tuning the laser wavelength or intensity [5,8]. The coupling can be explored in greater detail by measuring the temporal dependence of the fluorescence signal from the laser-split states at different laser wavelengths [9]. The Fourier transform of the acquired frequency-time data set results in the frequency map, displaying a typical image of the avoided level crossings, familiar from the Stark and Zeeman spectroscopy [10]. For optical transitions, the frequency map may also be measured directly, by changing the detuning of both the excitation laser and the coupling laser and detecting the total fluorescence yield at each setting [9], or by inspecting the population of the coupled state [11]. However, these approaches to the ATS characterization become very demanding or even unfeasible when dealing with short-lived states exhibiting lifetimes of the order of ps or shorter: the indirect approach requires temporal resolution of the emission events well below the lifetime of the excited states, and the direct approach relies on the tunability of short pulses over wide frequency intervals for both radiation sources while maintaining their spatiotemporal overlap at constant intensities.

In order to observe a significant splitting, the Rabi frequency must be comparable to or larger than the decay rate of the excited state, meaning that the laser intensity must stay above the critical value of $(8\pi\alpha|\mu|^2\tau^2)^{-1}$, at least until most of the exited atomic states have decayed. For atomic states with one or more inner-shell vacancies with lifetimes τ in the 1–10 fs range, the critical intensity is in the 10^{13}–10^{11} W cm^{-2} range, as seen by inserting above fine-structure constant α and a typical value of the coupling dipole matrix element $\mu \approx 1$ (in atomic units). Therefore, to keep the required laser power reasonably low, excitation pulses with duration significantly longer than τ should be avoided. A convenient source for studying short-lived states in the extreme-ultraviolet (EUV) spectral range is based on the high harmonic generation (HHG) [12].

In this work, we present an approach to constructing a two-dimensional frequency map and demonstrate its applicability on the case of selectively coupled atomic resonances with femtosecond lifetimes and tens of eV excitation energies. We show that the complete information about the optical coupling and pulse properties may be extracted from the map measured

 ©2019 American Physical Society

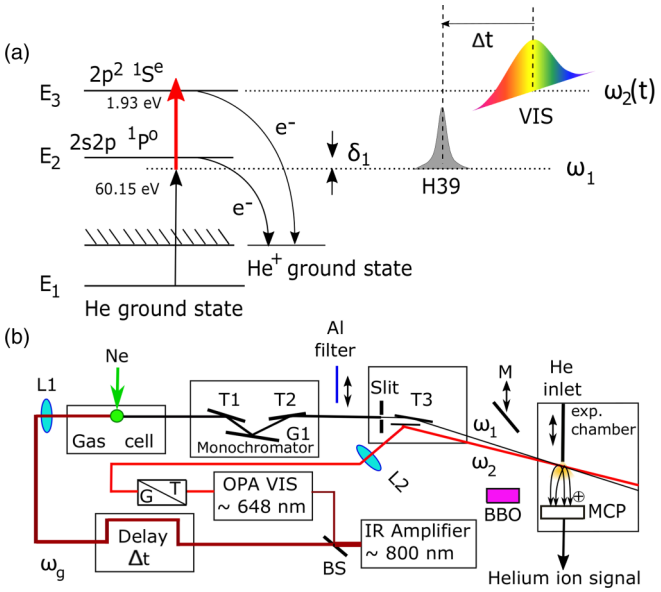

FIG. 1. (a) Three-level excitation and decay scheme with a delayed and detuned EUV pulse and a chirped VIS pulse. (b) Scheme of the experimental setup: a delayed NIR laser pulse (ω_g) is focused into the HHG gas cell filled with Ne. The monochromator selects the radiation ω_1. EUV pulse is focused on He gas target in the experimental chamber together with the VIS laser pulse ω_2, generated by the OPA and chirped by passing through the Glan-Taylor prism (G/T). Ions are collected by the MCP detector. $T_{1,2,3}$: toroidal mirrors; G_1: grating; $L_{1,2}$: lenses; *BS*: beam splitter. The removable Al filter, deflection mirror (M), and BBO crystal are used to align EUV and VIS pulses in time.

by scanning the frequency and delay of the excitation pulse, while keeping the settings of the laser coupling pulse fixed. An essential ingredient of the proposed method is a nonzero laser chirp: when combined with the delay, different frequencies of the laser pulse overlap with the excitation pulse frequencies at different times to imitate the laser frequency scan.

II. EXPERIMENT

The experiment was performed at the CITIUS light source at the University of Nova Gorica, Slovenia [13]. The spectrally purified HHG radiation pulse overlapped with the linearly chirped laser pulse, tuned to the $2s2p\ ^1P^o - 2p^2\ ^1S^e$ transition in helium. The total number of ions formed by autoionization was measured [Fig. 1(a)].

The setup consists of a HHG source, powered by an intense 800 nm Ti:sapphire laser producing 50 fs pulses with a 5 kHz repetition rate [Fig. 1(b)]. Prior to entering the gas cell, a 1.5 mJ laser pulse with a 30 nm bandwidth passed an adjustable delay line. The HHG radiation emitted by the Ne gas was filtered by a grating; at 1200 mm^{-1} groove density and 20 μm exit slit opening, the monochromator transmitted 60 eV photons with the 100 meV bandwidth. About one-half of the generating laser power was fed to the optical parametric amplifier (OPA) to produce VIS laser pulses tuned to 1.93 eV. The monochromatized HHG pulse, i.e., the EUV pulse and the linearly chirped VIS pulse crossed on the helium gas jet. He^+ ions were collected by a 40-mm-diameter MCP detector placed 5 cm below the tip of the gas needle.

A. EUV pulse

The HHG driving laser frequency was tuned until obtaining a good ion yield contrast due to the $2s2p\ ^1P^o$ excitation at 60.150 eV. In practice, the ratio of ions collected at the 39th harmonic (H39) and the 37th harmonic (H37) was maximized, with the former tuned to the resonance and the latter to the smooth ionization continuum at 3 eV lower photon energy (Fig. 2). The passage of the HHG radiation through the monochromator tilts the pulse front causing prolongation of the pulse [14]. With the known angular divergence of the HHG source, the monochromator ray tracing estimates about 115 fs time broadening resulting in an overall $\tau_1 = 125$ fs pulse duration on the target.

The monochromator resolution was estimated from the ratio of the measured ion yield and the scaled theoretical photoabsorption cross section of helium, convoluted by the monochromator bandwidth (Fig. 2). Taking 100 meV FWHM for the latter, the ratio results in a reasonable ion yield signal when assuming that the resonant structure in this energy range is entirely absent. In other words, if the monochromator broadening was smaller (larger), the expected signal at H39 would be too large (too small) with respect to the mean of the signal detected at H37 and H41. Indeed, the separate measurement of ion yield, using the same HHG source but N_2 gaseous target, resulted in H39 intensity roughly equal to the mean intensity of H37 and H41. This is expected because N_2 does not exhibit any resonant structure and displays a slowly varying photoionization cross section in the H37–H41 frequency region [15]. The EUV pulse broadening on the target was therefore substantially smaller than the width of the harmonic H39, roughly given by the width of the H37 ion yield peak in Fig. 2.

The number of photons in the pulse with the monochromator set to the H37 maximum was 1.2×10^5, as obtained from the measured ion count rate by assuming 1 mm target length and 10^{-4} mbar local target pressure, and taking 1.48 Mb for the helium photoionization cross section at 57 eV photon energy [16]. The lateral width of the EUV pulse at the target was not more than 0.15 mm, consistent with the observed ion yield trends when the gas needle was moved across the beam along both the perpendicular directions. The maximum H39 intensity in the target was then around $I_1 = 3 \times 10^4$ W cm^{-2}.

B. Linearly chirped VIS pulse

The VIS pulse maximum intensity was estimated by comparing the pulse energy, transmitted through the 0.3 mm pinhole, to the pulse energy measured without the pinhole. Assuming a radially symmetric Gaussian intensity profile, the result is consistent with the 0.3 mm beam waist in the target region and the maximum intensity $I_2 = (1 \pm 0.2) \times 10^{11}$ W cm^{-2} of the VIS pulse with 145 fs duration. This estimate accounts for the pulse-to-pulse instabilities and for the power losses due to the light scattering on the pinhole walls. Since the EUV beam waist was substantially narrower, the instantaneous VIS intensity was approximately

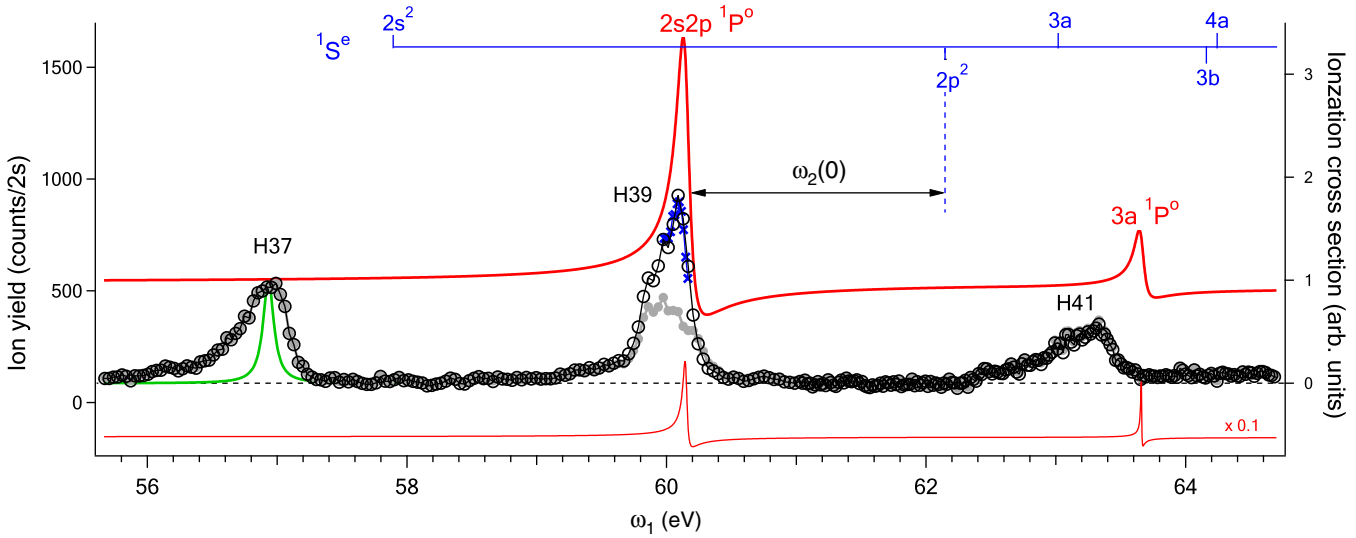

FIG. 2. Measured ion yield (empty black circles) as a function of the monochromator pass energy covering the $H37$–41 wavelength region with the coupling laser off. Thick (red) curve is the theoretical helium photoabsorption cross section [16], convoluted by a 100 meV FWHM Lorentzian (thick green curve) and scaled to 1 on the top of H37. Thin (red) curve denotes the shape of the unconvoluted cross section. The ratio of the measured ion signal (with background subtracted) and the convoluted cross section (full gray circles) estimates the ion yield signal for a fictitious case with no $2s2p\ ^1P^o$ resonance. The top bar gives energy positions of the lowest-lying $^1S^e$ resonances with dashed line showing the position of the $2p^2\ ^1S^e$ state. The ion yield signal observed in the limited range of the ATS measurement with a strongly delayed EUV pulse [Fig. 4(a)] is denoted by (blue) crosses.

the same at different lateral positions of the target ionization volume.

Time delay, at which the maximum temporal overlap of the VIS laser pulse and the EUV pulse occurs, was estimated by combining the VIS and the generating NIR laser pulses ($\omega_g = 1.55$ eV) on the BBO crystal placed at the same distance from the source as the gas target and illuminated by means of the switching mirror. Upon proper delay setting, the harmonic beam component with $\omega_g + \omega_2$ frequency was observed at the back side of the crystal.

With the OPA set to $\lambda = 648$ nm, the generated VIS laser pulses were 57 fs long and showed a nearly Gaussian intensity profile with the spectral width $\Delta\lambda = 25$ nm. Since this is significantly shorter than the duration of EUV pulses, the VIS pulses were prolonged to $\tau_2 = 145$ fs by passing through the Glan-Taylor polarizer with a thickness of $L = 25$ mm. According to the optical properties of the calcite [17], the passage generates 1305 fs^2 group delay dispersion (GDD) of the transmitted (extraordinary) ray. Formally, $g = L(d^2k/d\omega^2)$ is the weight of the lowest- (second-) order pulse-shape-changing term $(\omega - \omega_2)^2/2$ in Taylor expansion of the spectral phase [18]. The effect of such a linear chirp is to prolong a Gaussian pulse for a factor $\sqrt{1 + (4g \ln 2/\Delta\tau^2)^2}$ with respect to the Fourier limited pulse duration $\Delta\tau = 2\lambda^2 \ln 2/(\pi c \Delta\lambda) \approx 25$ fs. The expected pulse duration after the biprism is then 146 fs, which is very close to the measured value. However, this estimate neglects a possible intrinsic chirp of the OPA pulse, indicated by pulse duration exceeding $\Delta\tau$ for about a factor of two. The upper g limit may be obtained by adding 462 fs^2 to the calcite-only GDD value. This would reproduce duration of the OPA pulse, but would overestimate final pulse duration for 30% and still fail to explain slight deviations from the Gaussian profile at the OPA exit (nonlinear chirp). In the following, the VIS laser pulse chirp is approximated by $g = 1500 \pm 200$ fs^2 and the higher-order contributions, such as TOD and FOD, are neglected [18].

According to [19,20], the linear chirp in the time domain is defined by introducing linear dependence of the instantaneous angular frequency

$$\omega_2(t) = \omega_2(0) + 4\chi \ln 2\left(t/\tau_2^2\right) \tag{1}$$

by a dimensionless parameter χ. For a Gaussian pulse profile it can be shown that, given the temporal pulse width τ_2, the ratio of the spectral width of the chirped pulse intensity ($g \neq 0$) versus the corresponding Fourier spectral width ($g = 0$) is given by $\sqrt{1 + \chi^2}$. This leads to the following relation between the two chirp parameters: $\chi = 4g \ln 2/\Delta\tau^2$. The linear chirp parameter of the coupling laser pulse is thus estimated to $\chi = 7 \pm 1$, considering a relatively small but not precisely known GDD contribution from the OPA pulse. The laser frequency thus increases by a factor of $8\chi \ln 2/[\tau_2(E_3 - E_2)] \approx 8\%$ by the time the VIS pulse returns to one-half of its maximum intensity when the central laser frequency $\omega_2(0)$ corresponds to $E_3 - E_2$, the energy difference of the upper states.

III. THEORETICAL DESCRIPTION

Previous calculations dealt with the transmission of the EUV pump pulse as a function of the delay for different durations and intensities of the 800 nm laser coupling pulse [21,22] and, very recently, with simulations of two-color $2s2p\ ^1P^o$ (auto)ionization under the (near) resonant coupling conditions [23]. To simulate the present experimental

situation, the process was modeled by a three-level ladder scheme where the $2s2p\ ^1P^o$ autoionizing state at energy $E_2 = -0.693052$ a.u. is weakly coupled to the ground state of the helium atom at energy $E_1 = -2.903366$ a.u. by an EUV excitation pulse with frequency ω_1, and strongly coupled to the $2p^2\ ^1S^e$ autoionizing state at energy $E_3 = -0.621704$ a.u. by a linearly chirped VIS pulse with frequency $\omega_2(t)$ [Fig. 1(a)]. Introducing EUV delay Δt and VIS chirp χ to Eqs. (11)–(13) and (21) in Ref. [23], the problem is described by a set of equations for slowly varying amplitudes u_i for each of the three states:

$$i\dot{u}_1 = -i\gamma_1 u_1 + \frac{\Omega_{12}}{2}\left(1 - \frac{i}{q_{12}}\right)u_2, \tag{2}$$

$$i\dot{u}_2 = \left(-\delta_1 - i\frac{\Gamma_2}{2}\right)u_2 + \frac{\Omega_{12}^*}{2}\left(1 - \frac{i}{q_{12}}\right)u_1 + \frac{\Omega_{23}}{2}\left(1 - \frac{i}{q_{23}}\right)u_3, \tag{3}$$

$$i\dot{u}_3 = \left(-\delta_1 - \delta_2 - 4\chi\ \ln 2\frac{t}{\tau_2^2} - i\frac{\Gamma_3}{2}\right)u_3 + \frac{\Omega_{23}^*}{2}\left(1 - \frac{i}{q_{23}}\right)u_2. \tag{4}$$

The set is solved together with rate equation

$$\dot{y}_i = \gamma_1|u_1|^2 + \Gamma_2|u_2|^2 + \Gamma_3|u_3|^2 + 2\,\mathrm{Re}\left(\frac{\Omega_{12}^* u_1 u_2^*}{q_{12}} + \frac{\Omega_{23}^* u_2 u_3^*}{q_{23}}\right) \tag{5}$$

to calculate $y_i(t \to \infty)$, the asymptotic value of the ion yield. Above, $\delta_1 = \omega_1 - E_2 + E_1$ and $\delta_2 = \omega_2(0) - E_3 + E_2$ denote the detuning of the EUV pulse and of the central frequency of the VIS pulse, respectively. The autoionization rates of states 2 and 3 are given by $\Gamma_2 = 1.37 \times 10^{-3}$ a.u. and $\Gamma_3 = 2.13 \times 10^{-4}$ a.u., respectively. The direct ground-state photoionization rate $\gamma_1(t) = (\sigma_c/\omega_1)I_1 g_{\tau_1}(t - \Delta t)$ due to the Gaussian excitation pulse, $g_\tau(t) \equiv \exp[-4\ \ln 2(t^2/\tau^2)]$, is determined by the photoionization cross section $\sigma_c(\omega_1) = 1.4$ Mb, and results in a smooth background. The Fano parameters are $q_{12} = -2.76$ and $q_{23} = -2415$ [23]; the complex Rabi frequencies are defined as

$$\Omega_{12}(t) = \mu_{12}\sqrt{8\pi\alpha I_1 g_{\tau_1}(t - \Delta t)}e^{-i\omega_1 \Delta t},$$

$$\Omega_{23}(t) = \mu_{23}\sqrt{8\pi\alpha I_2 g_{\tau_2}(t)}e^{2i\chi\ \ln 2(t^2/\tau_2^2)},$$

and the dipole matrix elements are $\mu_{12} = 3.60 \times 10^{-2}$ a.u. and $\mu_{23} = 2.16$ a.u., respectively [23].

A general view on the chirp parameter dependence of results is presented in Fig. 3, where a series of calculated ion yield maps in the frequency-delay space is presented for seven different values of χ in the 0–50 range, together with the corresponding two-color ion yield map, calculated for the unchirped laser pulse ($\chi = 0$), fully overlapping in time with the EUV pulse. To sharpen the picture, the maps are plotted without considering the HHG monochromator broadening. In the map sequence one can clearly follow evolution of the ion yield signal from the symmetric, ring-shaped form at $\chi = 0$ with (vertical) gap orientation along the delay axis, to the slowly closing, quasihorizontal gap at $\chi = 50$ where the resonant spectral components in the chirped pulse exhibit a strongly reduced duration. In the simple view, the effect of the increasing linear chirp parameter on the ion yield map can be described by the gap rotation from the vertical (delay) to the horizontal (frequency) direction, as indicated by following a sequence of white lines on the frequency-delay maps in Fig. 3.

IV. RESULTS AND DISCUSSION

The ATS experiment was performed by measuring the helium ion yield at different delays of the EUV pulse with respect to the VIS pulse, covering ±400 fs range in steps of 25 fs around a predetermined zero-delay time. At each delay setting, the 2 s/point monochromator scan was taken in the narrow $2s2p\ ^1P^o$ resonance region. An average of 30 ion yield maps in Fig. 4(a) clearly shows a gap at small delays that intersects the ion signal ridge originating from the $2s2p\ ^1P^o$ ionization. Note that the previous two-color experiments dealt with the EUV transmission changes in the vicinity of the $2s2p\ ^1P^o$ autoionizing state in He at a relatively high intensity of the coupling laser pulses, considerably detuned from the resonant frequency [24].

To interpret the observations, two sets of calculations were performed: the first by varying frequency ω_1 and delay Δt of the EUV pulse with respect to the resonantly tuned and linearly chirped VIS pulse [Fig. 4(b)] and the second one by fixing the delay to zero and varying both, frequency ω_1 of the EUV pulse and frequency ω_2 of the *unchirped* VIS pulse, across the resonance region [Fig. 4(c)]. While the first set simulates experimental conditions, the second set corresponds to the ion yield in the frequency plane. Apart from the small frequency shifts, the latter reflects the basic ATS result: the two-level anticrossing following a pair of hyperbolas with the asymptotic behavior $\delta_1 = 0, -\delta_2$ and $\sqrt{\Omega_{\mathrm{eff}}^2 + \delta_2^2}$ splitting along the δ_1 axis [2]. The minimum splitting, extracted from Fig. 4(c), is $\Omega_{\mathrm{eff}} \approx 90$ meV. The ion signal is seen to jump from one level to the other in the vicinity of $\delta_2 \approx 0$, following the weight of the $2s2p\ ^1P^o$ resonance in the laser-coupled states: although the $2p^2\ ^1S^e$ resonance decays by autoionization too, it acts here as a dark state since its photoexcitation from the atomic ground state is dipole forbidden. Note that the gap in Fig. 4(c) does not cross the doubly resonant position $\delta_1 = \delta_2 = 0$ because of the strongly asymmetric absorption profile of the $2s2p\ ^1P^o$ state.

While the δ_1 axis covers the same frequency range F_1 in all the three maps, the frequency range $F_2 = 4\chi T\ \ln 2/\tau_2^2 \approx \pm 0.24$ eV on the δ_2 axis in Fig. 2(c) was chosen according to the linear chirp relation (1) to match the experimental delay range $T = \pm 400$ fs [Fig. 2(a)]. This scaling determines an angle the asymptotic $\delta_1 = -\delta_2$ makes with the δ_2 axis in Fig. 4(c). A good alignment of the asymptotic line with the observed signal gap in Fig. 4(a) indicates that the applied time-to-frequency scaling is reasonable. Conversely, at selected F_1 and T ranges, the gap inclination is given by angle $\phi = \arctan(k\chi)$, $k = (4\ \ln 2/\tau_2^2)(T/F_1)$, which can be taken as an indication of the linear chirp of the VIS pulse: when $\chi = 0$, the gap (slit) is vertical because the ion yield must be

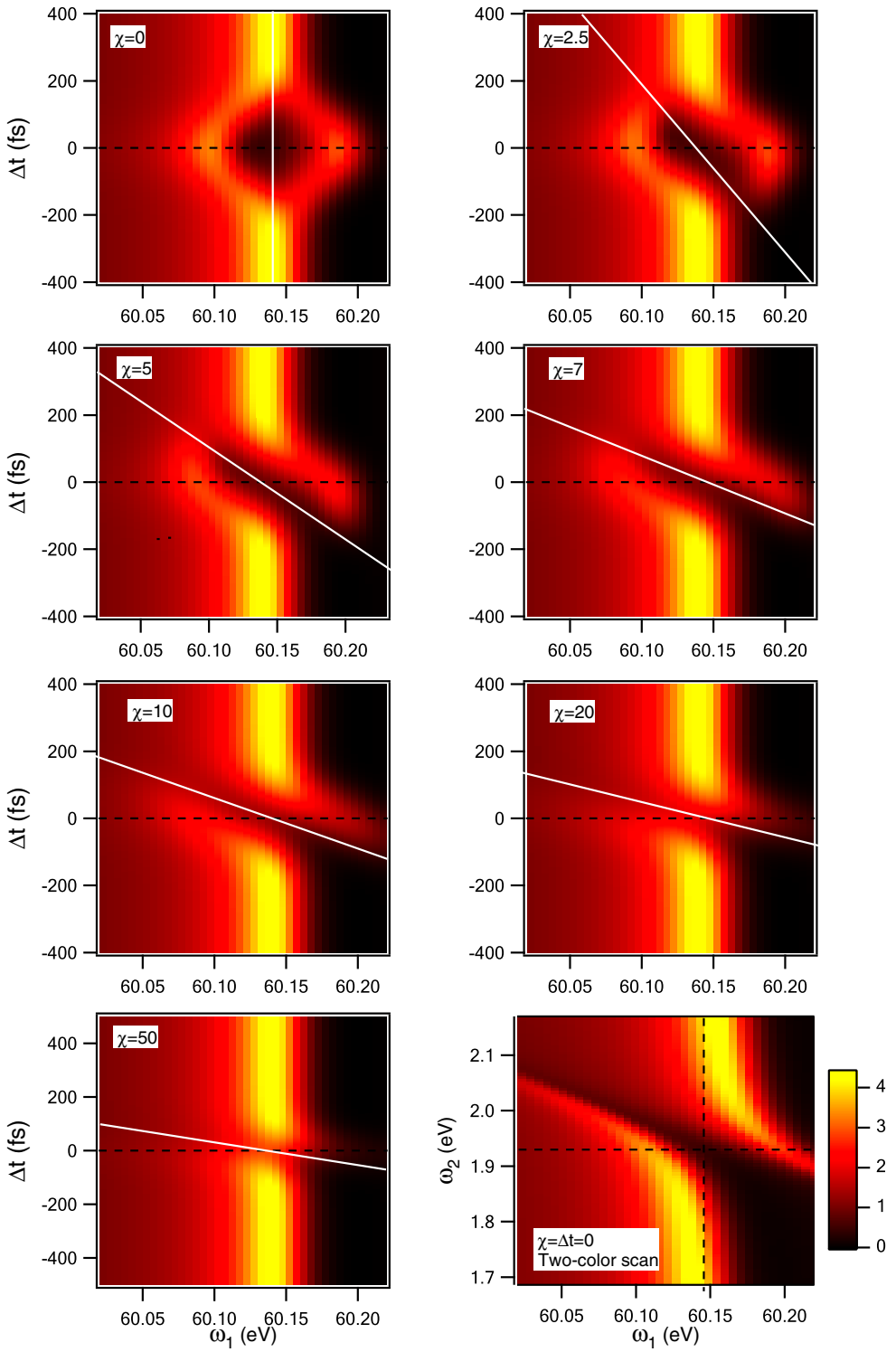

FIG. 3. Calculated frequency-delay ion yield maps for laser-coupled $2s2p\ ^1P^o$ and $2p^2\ ^1S^o$ resonances. The linear chirp parameters are $\chi = 0, 2.5, 5, 7, 10, 20, 50$. The EUV pulse has a maximum intensity $I_1 = 3.0 \times 10^4$ W cm^{-2} and 125 fs duration and the VIS laser pulse has a maximum intensity $I_2 = 10^{11}$ W cm^{-2} and 145 fs duration. The white line on each of the frequency-delay maps indicates the gap alignment. Presented is also the calculated two-color ion yield map for the unchirped laser pulse at zero delay.

the same when the unchirped Gaussian pulse is delayed or advanced by the same amount. Simulations with Eqs. (2)–(5) support this simple chirp dependence of the gap rotation angle (Fig. 3). The sense of rotation towards the horizontal axis depends on the sign of the linear chirp parameter. In our experiment, $\Delta t < 0$ means that the EUV pulse arrives after the laser pulse and the observed rotation is counterclockwise for $\chi > 0$ [Fig. 4(b)].

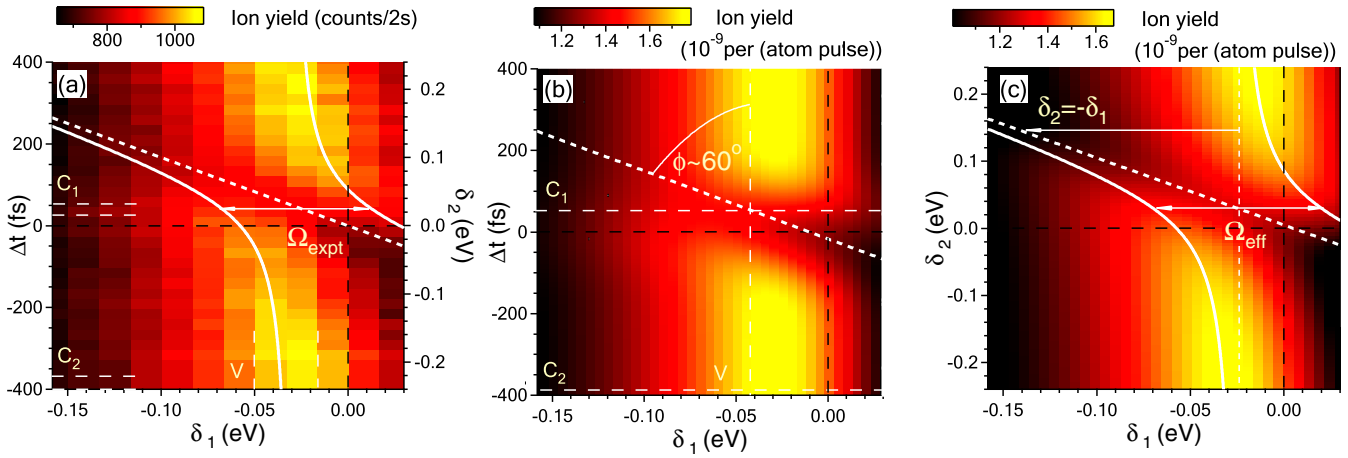

FIG. 4. (a) Ion yield map of the $2s2p\ ^1P^o$ resonance, measured as a function of the EUV pulse frequency detuning δ_1 from the 60.152 eV excitation energy and delay Δt with respect to the chirped VIS laser pulse, tuned to the $2s2p\ ^1P^o - 2p^2\ ^1S^e$ transition at 1.938 eV. The pairs of dashed white lines indicate signal integration area for the horizontal (C_1, C_2) and the vertical (V) cut, presented in Figs. 3(a) and 3(b), respectively. (b) Calculated frequency-delay map for the 125 fs EUV pulse with the maximum intensity $I_1 = 3 \times 10^4$ W cm^{-2}, broadened by a 100 meV Lorentzian and the 145 fs VIS laser pulse with the maximum intensity $I_2 = 10^{11}$ W cm^{-2} and linear chirp parameter $\chi = 7$. (c) Calculated two-color map for the same EUV pulse as in (b) and the *unchirped* VIS pulse of the same duration and intensity as in (b). The white dotted lines mark the asymptotes of the two-level avoided crossing, characterized by $\Omega_{\rm eff}$ minimum splitting and denoted by a pair of white curves.

For further analysis it is convenient to introduce the pulse-averaged Rabi frequency $\Omega_{\rm av} = A\Omega_{23}(0)$, where

$$A = \frac{\int_{-\infty}^{\infty} g_{\tau_1}(t)dt \int_t^{\infty} \sqrt{g_{\tau_2}(t')}e^{-\Gamma(t'-t)}\Gamma\, dt'}{\int_{-\infty}^{\infty} g_{\tau_1}(t)dt} \qquad (6)$$

is the proportionality factor to the maximum Rabi frequency $\mu_{23}\sqrt{8\pi\alpha I_2} \approx 100$ meV, reached at $t = 0$. The averaging takes into account that decaying population of excited states, created at different times in proportion to $I_1 g_{\tau_1}(t)$, is submitted to time-dependent intensity $I_2 g_{\tau_2}(t)$ of the coupling laser field. The minimum doublet splitting thus changes in time and is proportional to the "momentary" Rabi frequency which itself is proportional to the square root of laser intensity. Estimating decay time Γ^{-1} by the lifetime of the $2s2p\ ^1P^o$ resonance, $\Omega_{\rm av} = 84$ meV comes close to the value of $\Omega_{\rm eff}$, extracted from the two-color map in Fig. 4(c).

The fit of a simple two-state model to the observed ion yield in Fig. 4(a) gives $\Omega_{\rm expt} \approx 80$ meV for the minimum splitting. This tends to be smaller than $\Omega_{\rm eff}$ because, even with two pulses fully overlapping in time, only a portion of the chirped temporal profile contains frequencies $\omega_2(t)$ close enough to the resonant frequency $\omega_2(0)$ to cause an observable ion yield from both members of the split doublet. The effect can be roughly described by limiting the integration range in the denominator of (6) to the finite time interval $\pm u/2$ around the pulse maximum. Using the chirp relation (1), the integration range is approximately given by $u = \Delta E \tau_2^2/(4\chi\ \ln 2)$, where ΔE is the energy interval spanned by the ion yield gap along the δ_2 axis of the two-color map. Inserting $\Delta E \approx 100$ meV, about 10% drop of the averaged Rabi frequency is obtained, similar to the observation.

From Fig. 4(c) it is evident that at laser detuning larger than 0.2 eV, the ac Stark effect practically vanishes at the selected VIS intensity. This is confirmed by a separate calculation with the additional neighboring $^1S^e$ and $^1D^e$ resonances giving essentially unmodified results shown in Figs. 2(b) and 2(c). At large laser detuning, the coupling effects may be recovered by increasing the VIS pulse intensity but then the mixing with the other close-lying resonances cannot be neglected.

Figure 5(a) shows two horizontal cuts through the measured ion yield map, the first with VIS and EUV pulses overlapping in time (C_1) and the second with no overlap (C_2). A good match with the corresponding cuts from the calculated map [Fig. 2(b)] not only validates the model, but it also shows quite a weak sensitivity of the ATS on the chirp parameter. The remaining differences may be attributed to the absence of nonlinear chirp effects in the VIS pulse simulation, as well as to the approximations made regarding a spectrotemporal profile of the EUV pulse. The vertical cut through the experimental map matches very well the calculated cut, as well as the scaled EUV-VIS cross-correlation Gaussian profile exhibiting the width of $\sqrt{\tau_1^2 + \tau_2^2} \approx 190$ fs [Fig. 5(b)]. Knowing the VIS pulse duration, the EUV pulse duration can thus be estimated from the experimental data, except for very high chirp parameters where the gap tends to disappear (Fig. 3).

V. SUMMARY AND CONCLUSIONS

In conclusion, we have solved a critical problem of how to measure the frequency map when the coupled states decay on the femtoseconds time scale. Instead of scanning the laser coupling frequency that may easily induce the uncontrolled changes of the pulse focusing, timing, duration, intensity, and chirp, the delay between the excitation and the coupling

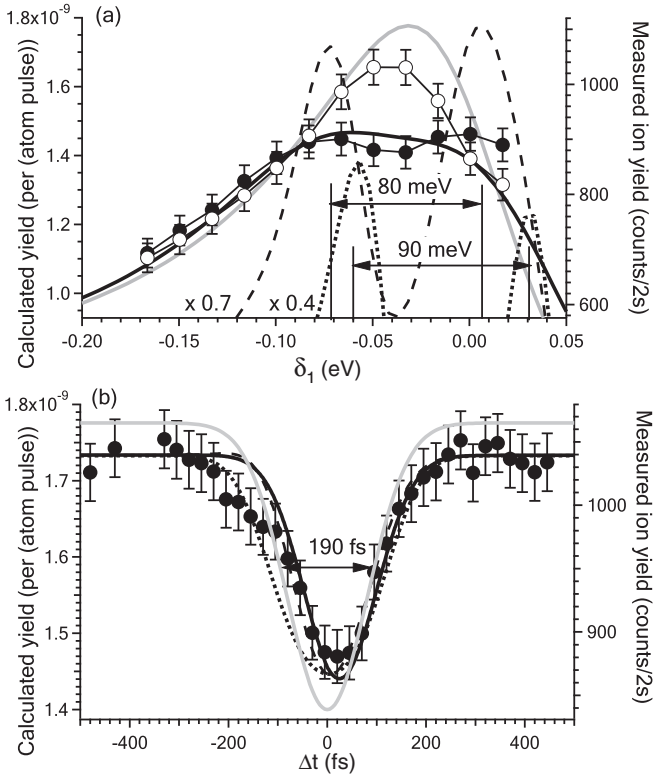

FIG. 5. (a) Horizontal cuts C_1 (connected black circles) and C_2 (empty connected circles) through the experimental map in Fig. 2(a) compared to the same cuts through the calculated ion yield map (black and gray thick curves). Dashed and dotted curves denote the calculated C_1 cut without the 100 meV broadening for $\chi = 7$ and $\chi = 0$, respectively. (b) Vertical cut V (black circles) through the experimental map compared to the calculated cut for $\chi = 7$ (black thick curve). Black dotted and gray full curves denote scaled results for the calculated $\chi = 0$ cut and the EUV-VIS cross correlation, respectively.

laser pulse is varied, so that all the laser settings remain fixed. We showed, experimentally and by numerical solutions of Schrödinger equation with predetermined pulse parameters and calculated atomic data, that the frequency-delay map closely resembles the frequency map of the ion yield, provided the coupling laser pulse is linearly chirped. The method was demonstrated on the paradigmatic case of the short-lived resonances in helium, but can be applied to an arbitrary decay channel of other laser-coupled states featuring femtosecond lifetimes. The proposed approach may be helpful to access properties of short-lived states with new properties optimized to certain applications, e.g., generation of femtosecond switches and transfer of decay into a desired dissociation channel, achievable only via population of highly excited states. Another important issue, resolved by such experiments, is the characterization of short EUV radiation pulses: when the two states with known properties are coupled by a well-characterized laser pulse, the excitation pulse parameters such as intensity, duration, and chirp can be extracted from the map. As an alternative to HHG, the laser-sliced synchrotron radiation sources provide short and tunable excitation pulses that may be well adapted to ATS experiments on laser coupled states at high excitation energies [25]. Finally, replacement of a simple ion counting device with an ion-selective detector makes the present approach appealing for molecular studies: a selective laser coupling of states populating different dissociation channels is a promising technique to disentangle and control molecular decay dynamics.

ACKNOWLEDGMENTS

This work is supported by the research Programme No. P1-0112 and by the research Project No. J1-8134 of the Slovenian Research Agency.

[1] F. Mahmood, C.-K. Chan, Z. Alpichshev, D. Gardner, Y. Lee, P. A. Lee, and N. Gedik, Nat. Phys. **12**, 306 (2016).
[2] C. N. Cohen-Tannoudji, in *The Autler-Townes Effect Revisited*, edited by R. Y. Chiao, Amazing Light (Springer, New York, 1996), Chap. 11, pp. 109–123.
[3] S. H. Autler and C. H. Townes, Phys. Rev. **100**, 703 (1955).
[4] K.-J. Boller, A. Imamoğlu, and S. E. Harris, Phys. Rev. Lett. **66**, 2593 (1991).
[5] H. A. Nguyen, T. Grange, B. Reznychenko, I. Yeo, P.-L. de Assis, D. Tumanov, F. Fratini, N. S. Malik, E. Dupuy, N. Gregersen, A. Auffèves, J.-M. Gérard, J. Claudon, and J.-Ph. Poizat, Phys. Rev. B **97**, 201106(R) (2018).
[6] B. Peng, S. K. Özdemir, W. Chen, F. Nori, and L. Yang, Nat. Commun. **5**, 5082 (2014).
[7] J. N. Becker, J. Görlitz, C. Arend, M. Markham, and C. Becher, Nat. Commun. **7**, 13512 (2016).
[8] K. Nozaki, T. Tanabe, A. Shinya, S. Matsuo, T. Sato, H. Taniyama, and M. Notomi, Nat. Photon. **4**, 477 (2010).
[9] Y. Zhou, A. Rasmita, K. Li, Q. Xiong, I. Aharonovich, and W.-b. Gao, Nat. Commun. **8**, 14451 (2017).
[10] R. D. Cowan, *The Theory of Atomic Structure and Spectra*, 1st ed. (University of California Press, San Diego, 1981), pp. 485–506.
[11] Y.-J. Chen, L. F. Gonçalves, and G. Raithel, Phys. Rev. A **92**, 060501(R) (2015).
[12] P. B. Corkum, Phys. Rev. Lett. **71**, 1994 (1993).
[13] C. Grazioli*et al.*, Rev. Sci. Instrum. **85**, 023104 (2014).
[14] L. Polletto*et al.*, Appl. Opt. **53**, 5879 (2014).
[15] G. R. Wight, M. J. V. der Wiel, and C. E. Brion, J. Phys. B **9**, 675 (1976).
[16] A. Mihelič, Ph.D. thesis, University of Ljubljana, 2006, http://www.rcp.ijs.si/amihelic/phd/thesis.pdf.
[17] G. Ghosh, Opt. Commun. **163**, 95 (1999).
[18] G. P. Agrawal, *Nonlinear Fiber Optics*, 3rd ed. (Academic Press, New York, 2001).
[19] B. E. A. Saleh and M. C. Teich, *Fundamentals of Photonics* (John Wiley & Sons, Inc., New York, 1991).
[20] A. Mihelič and M. Žitnik, Phys. Rev. A **91**, 063409 (2015).
[21] M. Tarana and C. H. Greene, Phys. Rev. A **85**, 013411 (2012).

[22] W.-C. Chu and C. D. Lin, Phys. Rev. A **87**, 013415 (2013).
[23] A. Mihelič, M. Žitnik, and M. Hrast, J. Phys. B **50**, 245602 (2017).
[24] Z.-H. Loh, C. H. Greene, and S. R. Leone, Chem. Phys. **350**, 7 (2008).
[25] T. E. Glover*et al.*, Nat. Phys. **6**, 69 (2009).